ACS OMEGA

http://pubs.acs.org/journal/acsodf Article

Chitosan-Grafted Polyacrylic Acid-Doped Copper Oxide Nanoflakes Used as a Potential Dye Degrader and Antibacterial Agent: In Silico Molecular Docking Analysis

Muhammad Bilal, Muhammad Ikram,* Tahira Shujah, Ali Haider, Sadia Naz, Anwar Ul-Hamid, Misbah Naz, Junaid Haider, Iram Shahzadi, and Walid Nabgan*

Cite This: *ACS Omega* 2022, 7, 41614−41626

Read Online

ACCESS | Metrics & More | Article Recommendations

ABSTRACT: This study examined the catalytic and bactericidal properties of polymer-doped copper oxide (CuO). For this purpose, a facile co-precipitation method was used to synthesize CuO nanostructures doped with CS-g-PAA. Various concentrations (2, 4, and 6%) of dopants were systematically incorporated into a fixed amount of CuO. The prepared samples were analyzed by different optical, structural, and morphological characterizations. Field emission scanning electron microscopy and transmission electron microscopy micrographs indicated that doping transformed CuO's agglomerated rod-like surface morphology to form nanoflakes. UV−vis spectroscopy revealed that the optical spectra of the samples exhibit a redshift after doping, leading to a decrease in band gap energy from 3.3 to 2.5 eV. The purpose of the study was to test the catalytic activity of pristine and CS-g-PAA doped CuO for the degradation of methylene blue in acidic, basic, and neutral conditions using $NaBH_4$ as a reducing agent in an aqueous medium. Furthermore, antibacterial activity was evaluated against Gram-positive and Gram-negative bacteria, namely, *Staphylococcus aureus* (*S. aureus*) and *Escherichia coli* (*E. coli*). Overall, enhanced bactericidal performance was observed upon doping CS-g-PAA into CuO, i.e., 4.25−6.15 and 4.40−8.15 mm against *S. aureus* and 1.35−4.20 and 2.25−5.25 mm against *E. coli* at the lowest and highest doses, respectively. The relevant catalytic and bactericidal action mechanisms of samples are also proposed in the study. Moreover, in silico molecular docking studies illustrated the role of these prepared nanomaterials as possible inhibitors of FabH and FabI enzymes of the fatty acid biosynthetic pathway.

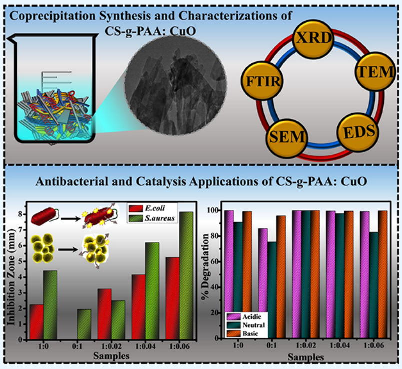

1. INTRODUCTION

Human beings are concerned about the future of the earth and its biodiversity. Rapid technological and industry advancements have resulted in many environmental threats, especially in terms of water contamination.[1] The primary cause of aquatic pollution is wastewater, which comprises a diverse range of synthetic dyestuffs from paper, leather, textiles, plastic, and mineral processing industries.[2−4] Synthetic dyes with an annual production of 7×10^5 metric tons are prominent contaminants that cause ecological imbalances in aquatic habitats.[2,5] Water pollution with these colored chemicals lowers solar penetration in the water, resulting in reduced water-based photosynthesis, increasing the chemical oxygen demand, and ultimately deteriorating the water ecosystem and food chain poisoning.[6−8] The cationic dye molecule methylene blue (MB) is widely employed in textile and other industrial applications. MB molecules are highly stable and decompose anaerobically to produce mutagenic and carcinogenic intermediates.[9] Furthermore, drug resistance in various pathogens against frequently used antibiotics has prompted the quest for alternative bactericidal substances.[10] Consequently, simultaneous elimination of organic pollutants found in wastewater streams, such as pesticides, phenolic compounds, dyes, and bacteria, could efficiently replace traditional staged treatment approaches.

Several biological, physical, and chemical solutions have been developed to address this environmental concern. Among them, chemical reduction provides the simplest, most rapid, and most effective way of eliminating dyes from aqueous solutions.[11] MB is particularly sensitive to redox activities because it turns blue when oxidized and disappears when reduced.[12] Chemically, water treatment agents are categorized as organic and inorganic. The advantages of inorganic remedial agents over organic remedial agents are their adaptability to harsh chemical properties and the high temperature of polluted streams, which make them preferable for wastewater treat-

Received: August 31, 2022
Accepted: October 26, 2022
Published: November 4, 2022

ment.[11,13,14] Inorganic agents such as metal and metal oxide nanomaterials with potential antibacterial and catalytic capabilities for dye degradation have attracted much attention. Consequently, nanomaterials have been extensively studied for their synthesis, properties, and uses in various fields, including chemistry, physics, biology, and engineering.[10] Nanostructured materials, defined as having a grain size of 100 nm or less and a significant surface area, have been shown to display unexpected features not seen in their coarse-grained analogues. The nanomaterial-based catalytic degradation of hazardous dyes has gained considerable interest among researchers as a potential solution to the rapidly evolving problem of environmental contamination from wastewater.[15,16]

Copper oxide (CuO) is an inexpensive and valuable semiconductor material with outstanding physiochemical properties, including antibacterial, antioxidant, low cost, and non-toxicity.[17] In addition, this metal oxide has prospective applications in water purification, biomedicine, biosensors, and electrodes.[18] Transition metal-doped CuO improves photocatalytic activity by preventing photoinduced electron−hole recombination.[19,20] The general properties of CuO nanoparticles are dependent on their morphological characteristics; accordingly, the development of doped CuO to enhance the catalytic and bactericidal activities remains a challenge.[21] In recent years, CuO has been doped with several elements, resulting in improved catalytic and antibacterial activities of the product.[22−26] The composites made with metal nanoparticles and polymers have a superior antimicrobial effect, leading to greater practical applications.[27] The formation of composites combines the key features of two or more polymers or a polymer blend with transition metals, resulting in a high adsorption capacity.[28] CuO has proven to be an efficient inorganic catalytic and bacterial agent in the presence of potential biopolymers having antibacterial and dye degradation properties.[29,30] Recently, Mallakpour et al. reviewed the structure, characteristics, and utilization of polymer/CuO nanocomposites.[18] The findings show that few researchers have examined the catalytic and antibacterial activity of CuO doped with polymers.

Biopolymers are eco-friendly alternatives to synthetic nonbiodegradable polymers. However, their regeneration and lower reusability limit their applications, which can be improved by producing their composites and doping.[31] Chitosan (CS) is a naturally occurring, widely spread polysaccharide derived from chitin (the second most abundant biopolymer).[32] Further, it exhibits a high capacity to eliminate pollutants from water, significantly exceeding that of activated carbon.[33] Polyacrylic acid (PAA) is also a commercially cost-effective polymer produced by combining acrylic acid monomers.[34] PAA behaves as an anionic polymer in water due to the loss of protons.[35] It also acts as a super-adsorbent polymer, which makes it helpful in removing organic pollutants. The PAA with a high carboxylic group density could improve the hydrophilicity of the resultant nanocomposite.[34] CS with functional groups −OH and $-NH_2$ is grafted to hydrophilic vinyl monomers via polymerization. Several studies have used chitosan-grafted polyacrylic acid (CS-g-PAA) for various environmental and biomedical applications such as cancer treatment and heavy metal ion removal.[36−39] Here, we employed CS-g-PAA doped CuO to examine the catalytic and dye degradation abilities of doped materials.

For nanomaterial synthesis, various techniques described in the literature are thermal reduction, chemical vapor deposition, microwave irradiation, and photochemical synthesis.[40−43] Among them, co-precipitation is an efficient method regarding yield, product purity, cost, and reproducibility.[44]

The objective of this research was to synthesize pristine CuO, CS-g-PAA, and (2, 4, and 6%) doped CuO nanomaterials via the co-precipitation route and evaluate their structural, optical, and morphological properties along with catalytic activity and antimicrobial behavior. As-prepared nanomaterials were tested for catalytic activity against the MB dye and bactericidal potential against Gram-positive and Gram-negative bacteria, i.e., *Staphylococcus aureus* and *Escherichia coli*. Further, molecular docking predictions were performed against selected enzyme targets, i.e., enoyl-[acyl-carrier-protein] reductase (FabI) and β-ketoacyl-acyl carrier protein synthase III (FabH) from *E. coli* and *S. aureus* to evaluate inhibition potential of these synthesized products.

2. EXPERIMENTAL PART

2.1. Materials. Copper dichloride ($CuCl_2$), NaOH, sodium borohydride ($NaBH_4$), chitosan (CS), and polyacrylic acid (PAA) (products of Sigma-Aldrich, Germany) were used.

2.2. Synthesis of Chitosan-*g*-polyacrylic Acid-Doped Copper Oxide. CuO nanoflakes (NFs) were prepared with one-pot chemical co-precipitation, as shown in Figure 1. $CuCl_2$ (0.5 M) was used as a Cu source, and the solution was heated at 60−70 °C under constant stirring. CS-g-PAA was synthesized using the previously reported route.[45] To achieve the doping effect of CS-g-PAA into CuO NFs, 2, 4, and 6% of CS-g-PAA were incorporated into the above stirred CuO solution. Following that, NaOH (0.5 M) was employed to maintain the pH at 12 while continuously stirring for 1 h. Achieved supernatants were collected with centrifugation (7500 rpm for 6 min). After washing multiple times with DI water and drying at 150 °C overnight, the final product was obtained.

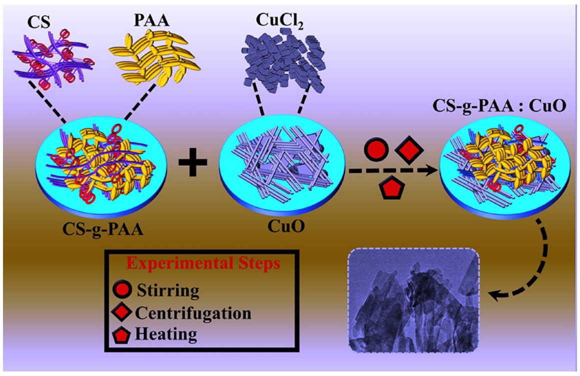

Figure 1. Synthesis route for CuO, CS-g-PAA, and CS-g-PAA (2, 4, and 6%) doped CuO NFs.

2.3. Catalytic Activity. The catalytic performance of CuO, CS-g-PAA, and doped CuO was investigated by way of degradation of the MB dye (that acts as an oxidizing agent) into lucomethylene blue (LMB) with reducing agent $NaBH_4$ while CuO acts as a nanocatalyst. The initial reference sample was prepared by adding 400 mL of $NaBH_4$ (0.1 M) solution into 3 mL of aqueous MB in a quartz cell. Afterward, 400 mL of CuO, CS-g-PAA, and doped CuO NFs was added to the preceding solution. The reaction rate was indicated by decolorization and changes in dye absorption intensity in the absence of light. A wavelength of 665 nm is the characteristic maximum absorption of MB, so it was used to monitor the reduction in UV−vis absorption. The degradation efficiency was computed as

$$\%\text{degradation} = \left(\frac{C_0 - C_t}{C_0}\right) \times 100$$

where C_o and C_t are the initial and certain time absorptions.

2.4. Antimicrobial Evaluation. The antibacterial performance was investigated by swabbing 1.5 × 10^8 CFU mL^{-1} isolated stains (G+ve and G−ve) on MacConkey agar (MA) and mannitol salt agar (MSA) plates, respectively, using a well diffusion assay. Samples of sheep (ovine) milk exhibiting signs of clinical mastitis were acquired from local farms in Punjab (Pakistan) and grown at 5% blood agar. To isolate *E. coli* and *S. aureus*, cultivated isolates were streaked in triplets on MA and MSA. A sterile cork borer was used for 6 mm wells on plates, and samples were incorporated at lowest (0.5 mg/0.05 mL) and highest (1.0 mg/0.05 mL) doses. The positive (+ve) and negative (−ve) control concentrations were used (0.005 mg/0.05 mL and 0.05 mL, respectively) for ciprofloxacin and distilled water. The loaded Petri dishes were incubated overnight at 37 °C, and bactericidal activity was determined by measuring inhibition zones with a Vernier caliper.

2.4.1. Investigation of Minimum Inhibitory Concentration Test. Using the typical twofold serial dilution procedure in broth, the minimum inhibitory concentrations (MICs) of CuO, CS-g-PAA, and doped CuO NFs were determined. In this investigation, *E. coli* and *S. aureus* strains were matured in broth for 18 h at 37 °C. The McFarland standard for turbidity in *E. coli* and *S. aureus* suspensions was set at 0.5. To create the inoculums, the solution was subsequently diluted 1:10 with 10^7 CFU/mL broth. Dissemination concentrations of CuO, CS-g-PAA, and doped CuO began at 100 mg/L and were serially diluted twice. The serial twofold dilution solution was then emptied into sterile tubes and injected with bacterial suspensions under aseptic conditions. In each instance, the MIC was defined as the lowest bactericidal concentration that suppressed observable growth after 18 h of incubation at 37 °C.

2.5. Molecular Docking Studies. Molecular docking studies of these NFs were performed against selected enzyme targets belonging to fatty acid biosynthetic pathways, i.e., enoyl-[acyl-carrier-protein] reductase (FabI) and *β*-ketoacyl-acyl carrier protein synthase III (FabH) from *E. coli* and *S. aureus*. 3D crystal structures of selected enzymes were obtained from the Protein Data Bank with PDB ID as 5BNM (Res: 1.7 Å) for $FabH_{E.\ coli}$,[46] 1MFP (Res: 2.33 Å) for $FabI_{E.\ coli}$,[47] and 6TBC (Res: 2.55 Å) for $FabI_{S.\ aureus}$.[48] The molecular docking predictions were done using ICM v3.8-7d (Molsoft L.L.C., La Jolla, CA)[49] where enzyme structures were prepared using the receptor preparation tool of ICM.

The water molecules alongside native ligands were removed, polar H-atoms were added in each case, and finally, energy was minimized. The binding pocket was specified using grid box dimensions within 5 Å vicinity of the native ligand. Top-ranked docked complexes were generated in each case, and the best were selected for further analysis. The 3D view of binding interactions was generated using PyMOL software. The ligedit tool of ICM Molsoft was used for ligand structure preparation.

3. RESULTS AND DISCUSSION

The obtained XRD spectra (Figure 2a) of synthesized samples provide information related to phase and crystallite size. The peaks at 2θ = 34.9, 38.4, 53.2, 57.7, 61.1, 65.2, and 66.9° refer to (0 0 2), (1 1 1), (0 2 0), (2 0 2), (1 1 $\bar{3}$), (0 2 $\bar{2}$), and (1 1 3) planes of monoclinic symmetry (space group C12/*c*, JCPDS: 96-410-5683), respectively, and characteristics of the Cu_4O_4 monoclinic structure with lattice parameters *a* = 4.571 Å, *b* = 3.327 Å, and *c* = 5.177 Å along with $\alpha = \gamma = 90°$, and β = 98.640°.[50] The calculated cell density and volume were 6.45 g/cm^3 and 78.73 $Å^3$, respectively. Peaks at 31.8 and 48.0° were identified as (2 0 0) and (2 0 4) planes of CuOH and Cu_4O_3, respectively (JCPDS: 00-042-0638/00-033-0480). This occurrence of more than one phase of CuO is reported in the literature.[51,52] In the XRD spectrum of CS-g-PAA, the macromolecular chain grafting reaction onto the chitosan backbone is demonstrated by a peak around 21°.[53] The CS peak observed in the literature[54] around 20° vanished in the grafted structure, which is related to a weakening of the hydrogen bonding interaction between hydroxyl and amino groups of CS macromolecules due to the side chains' stereochemical hindrance or diminished group concentrations. PAA chain conformational hindrance and bulkiness produce disorder in structures as polymeric materials refer to amorphous systems, but the effect of PAA was not substantial at low temperatures.[55,56] Peak shifts toward 35.5 and 38.5° confirm the dopants in CuO.[57] Moreover, the lattice parameters of the 6% sample increase with a decrease in crystallite size as *a* = 4.897 Å, *b* = 5.952 Å, and *c* = 8.852 Å, while the unit cell volume grew to 258.00 $Å^3$ having a density of 1.55 g/cm^3. The Debye−Scherrer equation $\left(D = \frac{k\lambda}{\beta\cos\theta}\right)$ gives the average crystallite sizes of CuO, CS-g-PAA, and CS-g-PAA (2, 4, and 6%) doped CuO as 28.8, 18.4, 22.1, 19.2, and 19.5 nm, respectively. The strong interaction of the cationic dopants with the CuO nanomaterial reduces the size of resultant nanomaterials. Sample crystallinity is reflected from peak intensities, and broad peaks reveal that the synthesized material has a smaller crystallite size.[58]

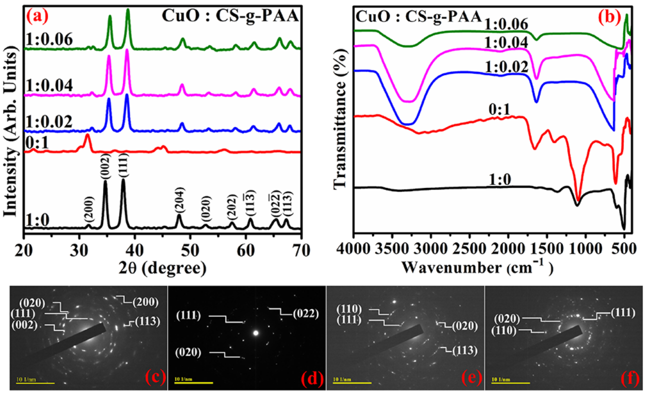

Figure 2. (a) XRD pattern of CuO (1:0), CS-g-PAA (0:1), and CS-g-PAA (2, 4, and 6%) doped CuO (1:0.02, 1:0.04, and 1:0.06); (b) FTIR spectra and SAED profile of (c) 1:0, (d) 1:0.02, (e) 1:0.04, and (f) 1:0.06.

The chemical structure was analyzed using an FTIR spectrometer within a wavenumber range of 4000 and 400 cm^{-1}, as represented in Figure 2b. The broadband in the 3200−3550 cm^{-1} region appeared from aromatic, aliphatic H-bonded, and −OH, C−O, and O−H surface hydroxyl group stretching vibrations from adsorbed water molecules, attributed to the fact that nanocrystalline materials with a large surface-to-volume ratio absorbed the moisture.[59] The peak at 1639 cm^{-1} indicates the Cu−O bond stretching of CuO nanomaterial, and the 1377 cm^{-1} peak shows CO_2, usually adsorbed on the surface of materials from the air.[60] The peak around 1114 cm^{-1} refers to −OH bending vibrations of Cu−OH as confirmed with XRD.[61] The Au and Bu modes of CuO can be attributed to peaks shown at 432.3, 497, and 603.3 cm^{-1}.[62,63] The Cu−O stretching along the [101] direction can be associated with the high-frequency mode at 603.3 cm^{-1}, whereas the peak at 497 cm^{-1} is also related to the Cu−O stretching vibration along the [101] direction.[62]

The production of NH^{3+} groups was linked to the development of new peaks in the CS-g-PAA FTIR spectrum at 1640 cm^{-1}, and COO^- group asymmetric stretching was observed around 1410 cm^{-1}. These findings indicated the dissociation of PAA carboxylic groups to COO^- groups, which then interacted electrostatically with protonated amino groups from CS. The presence of CS in the nanomaterial showed skeletal vibrations at 1082 cm^{-1} involving C−O stretching.[64] Upon doping, the peak appearance at 1635 cm^{-1} confirmed the presence of dopants in CuO.

As shown in Figure 2c−f, SAED patterns showed discrete and bright rings in samples parallel to various planes of pristine and doped CuO. These findings attributed to poly-crystallized materials are in good agreement with XRD data.

UV−vis spectrophotometry revealed the optical spectra of synthesized nanomaterials in the 200−600 nm range (Figure 3a). The peak appearance in the absorption range between 250 and 300 nm is assigned to CuO formation.[65] CuO surface plasmon vibration excitation generated an absorption peak at 294 nm.[66] PAA strong absorption below 235 nm[67] and the CS absorption peak at 208 nm[68] shifted to 340 nm in the grafted structure. The Tauc plot was constructed to estimate the optical band gap (Eg) through straight-line part extrapolation toward the x axis presented in Figure 3b. The redshift in band gap energy from 3.3 eV (376 nm)[69] in pristine CuO to around 2.5 eV (496 nm) in the case of CS-g-PAA specific concentration (2, 4, and 6%) doped CuO is attributed to the quantum confinement effect (see Figure 3b). This alteration in the optical band gap and crystallinity within the doped CuO confirms the complexation and interaction between dopants and CuO.

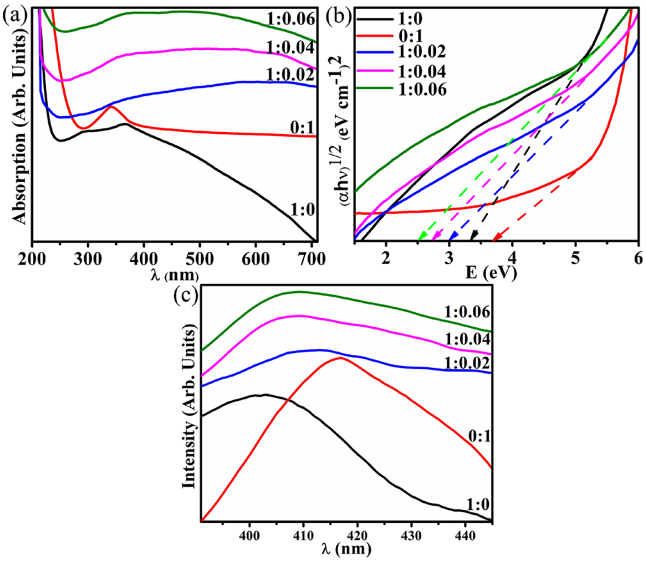

Figure 3. CuO:CS-g-PAA: (a) optical spectra, (b) band gap energy determination, and (c) photoluminescence emission spectra.

The PL spectra of samples are presented in Figure 3c. CuO luminescence properties are morphology-dependent as recombination of electrons linked to a donor, and free holes are induced by defects in materials, including impurities or vacancies.[70] Furthermore, high PL emission intensity after incorporating dopants indicates higher recombination rates since the electron−hole pair recombination rate is proportional to intensity. Oxygen with interstitial oxygen transition vacancy causes the luminescence bands in the violet-blue range (400−402 nm).[71] These oxygen vacancies play their role in bacterial activity via higher-level production of hydroxide radicals, singlet oxygen, and other reactive oxygen species (ROS) in the cell cytoplasm.[72] CS-g-PAA doped samples exhibit greater PL emission broadness, indicating vacancies in conjunction with singly ionized oxygen deep-level structural defects.

To investigate the surface morphology of CuO, CS-g-PAA, and the effect of (2, 4, and 6%) CS-g-PAA doped CuO, field emission scanning electron microscopy (FE-SEM) and transmission electron microscopy (TEM) were used. FE-SEM and TEM images of CuO with strong agglomeration and irregularly shaped rods oriented in different directions are shown in Figure 4a,a′. The formation of an agglomerated irregular spherical shape was revealed by CS-g-PAA (Figure 4b,b′). Figure 4c−e,c′−e′ shows that CS-g-PAA forms a NF-like morphology on the surface of NFs. These figures indicate that

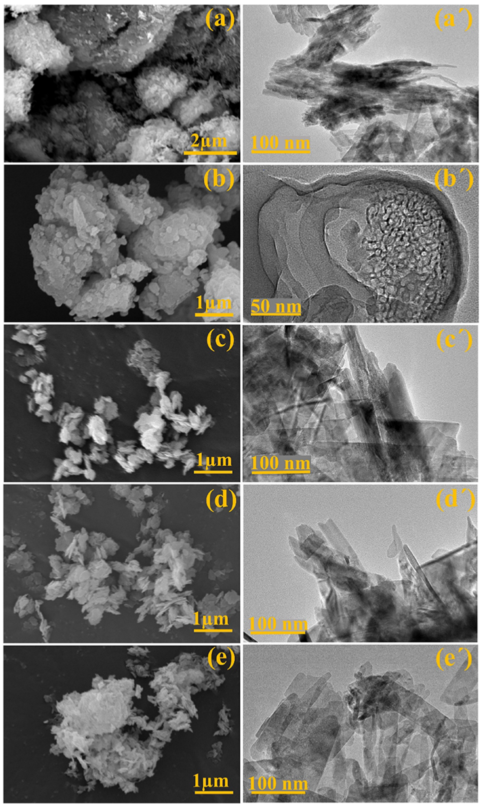

Figure 4. FE-SEM and TEM images of CuO:PAA: (a, a′) 1:0, (b, b′) 0:1, (c, c′) 1:0.02, (d, d′) 1:0.04, and (e, e′) 1:0.06.

https://doi.org/10.1021/acsomega.2c05625
ACS Omega 2022, 7, 41614−41626

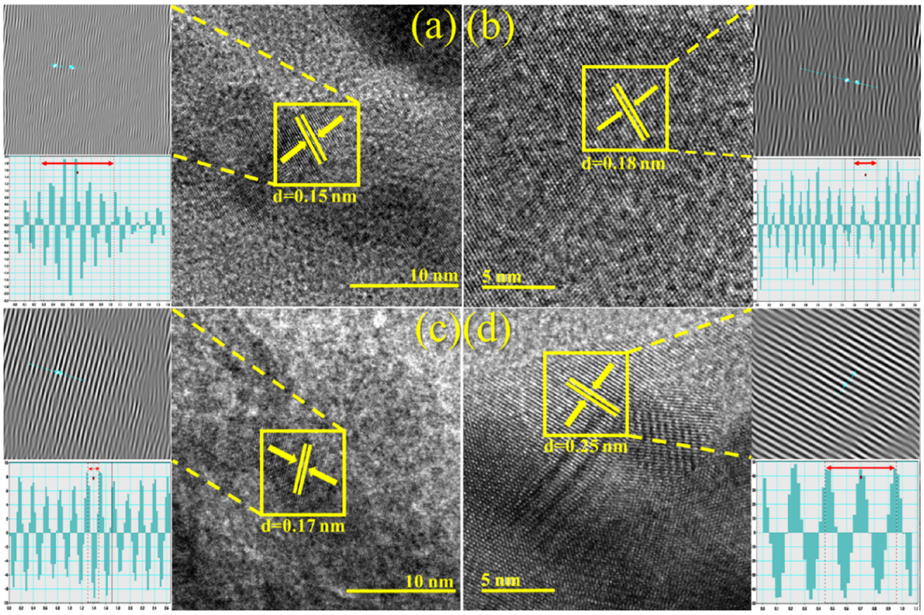

Figure 5. d-spacing calculated from HR-TEM images of CuO:CS-g-PAA: (a) 1:0, (b) 1:0.02, (c) 1:0.04, and (d) 1:0.06.

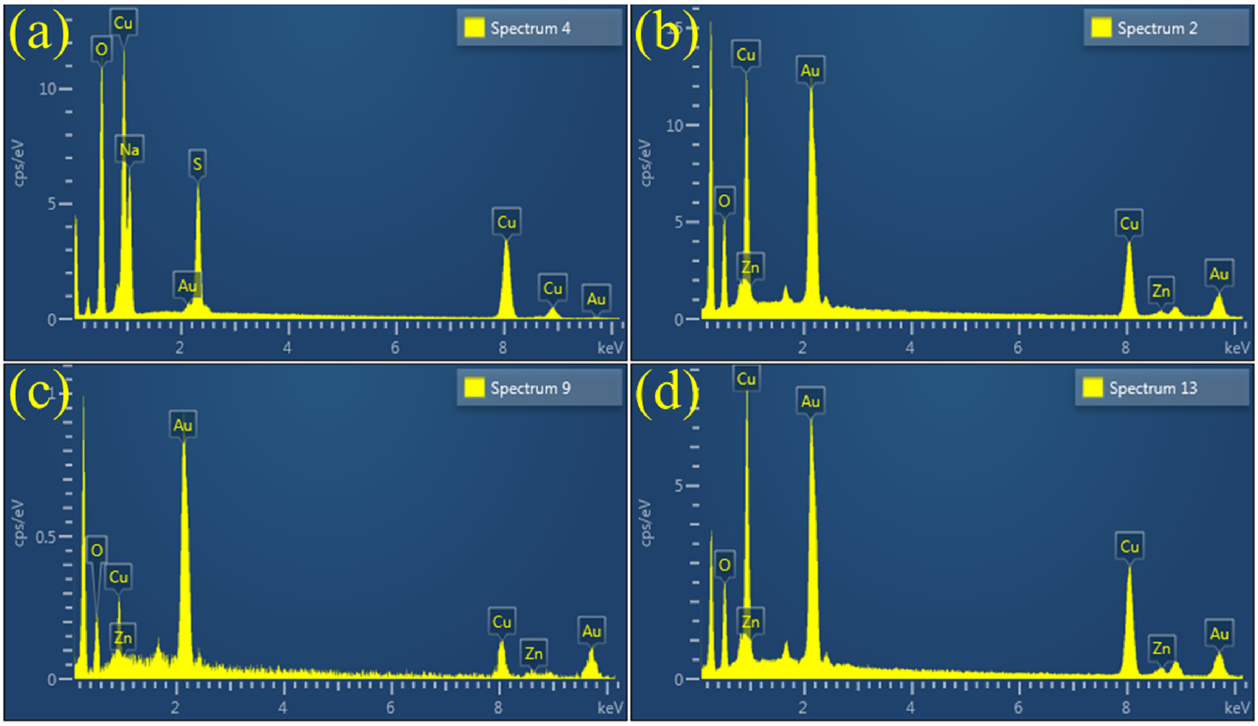

Figure 6. EDS of CuO:CS-g-PAA: (a) 1:0, (b) 1:0.02, (c) 1:0.04, and (d) 1:0.06.

with a high concentration of CS-g-PAA, white spots of different sizes are visible on the surface of CuO. After doping, aggregation of NFs occurred, but as the doping concentration increased, agglomeration of NFs resumed. Furthermore, this observation is linked to the significant interaction of the cationic nature of dopants with negatively charged surfaces of CuO.[45]

High-resolution TEM (HR-TEM) analysis of edge regions is a direct method to estimate the number of layers microscopically. On a single grain, HR-TEM images demonstrate different atomic planes with periodic atomic arrangements, as shown in Figure 5a−d. Furthermore, planes are well ordered to create a single layer at specific locations, where interplanar spacing is measured at 0.15 nm. This matches up with the (2 0 2) facet of the monoclinic CuO phase following XRD analysis. The d-spacings of doped samples were determined to be 0.18, 0.17, and 0.25 nm upon adding dopants compatible with the XRD pattern.

The elemental composition of obtained nanostructures was examined through EDS results, as illustrated in Figure 6a−d. Cu and O peaks confirmed the presence of CuO. The Na peak also appeared because NaOH was incorporated during synthesis to adjust the pH of the samples. Samples coated with a Au coating were used to prevent surface charge and

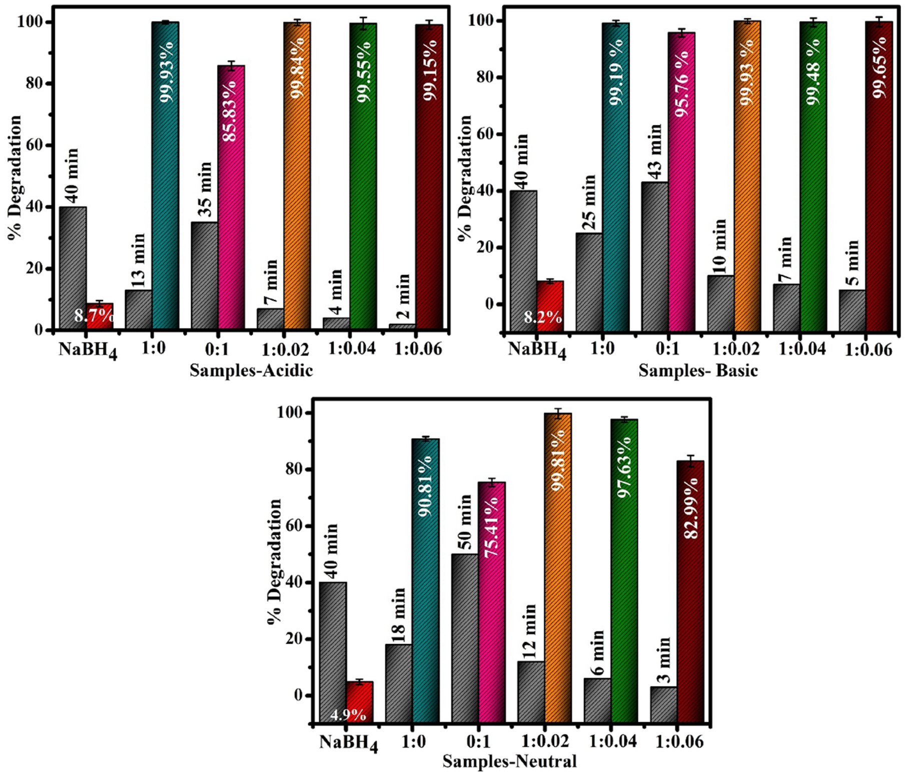

Figure 7. Catalytic activity in the presence of $NaBH_4$ (without a catalyst) and with catalyst CuO:CS-g-PAA.

facilitate secondary electron emission. The specimen was sputtered with Au to provide even conductivity with a homogeneous surface for imaging and analysis. Aluminum, silver, and carbon can all be used to coat specimens. On the other hand, gold is a great conductor that does not oxidize, making it the preferred conductive metal for coating in research laboratories. As a consequence, small Au peaks are observed in the EDS spectra.

To examine catalytic activity against MB with reducing agent $NaBH_4$, pristine CuO, CS-g-PAA, and doped CuO nanocatalysts were utilized. CuO, CS-g-PAA, and (2, 4, and 6%) doped CuO nanomaterials showed maximum degradation of 90.81, 75.41, 99.81, 97.63, and 82.99% in neutral (pH = 7), 99.93, 85.53, 99.84, 99.55, and 99.15% in acidic (pH = 4), and 99.19, 95.76, 99.93, 99.84, and 99.65% in basic media (pH = 12). The acquired results were compared to Degussa P25 TiO_2 data from the published literature reported by Tichapondwa et al., demonstrating 81.4% degradation of the MB.[73] The Degussa P25 TiO_2 powder was highly crystalline, with 80.3% anatase and 19.7% rutile composition. Without a catalyst, dye degradation reached maxima of 4.9, 8.2, and 8.7% in 40 min in neutral, basic, and acidic media, respectively, as shown in Figure 7. In consonance with obtained data, when MB was degraded at pH = 7, the catalytic activity of 2% doped CuO improved and then decreased with increasing doping concentration, eventually falling below that of undoped samples. This is attributed to CuO nanostructures showing different efficiency and degradation rates with changing morphologies.[74] The surface area and pore size of CuO were calculated to be 9.3 ± 0.5 and 2.1 ± 0.2, respectively, by Shrestha et al.[75] Furthermore, with CS doping, Srivastava et al. reported that the surface area and pore size of CS/CuO nanocomposites were 15.844 m^2/g and 1.22 nm, respectively, showing that the adsorptive properties of nanocatalysts increase due to the large surface area.[76] Thus, increased catalytic activity may be due to the well-defined large surface area of CuO nanostructures. Conversely, an excessive amount of dopants can take up residence in the active sites of CuO, which slows down the adsorption process. In general, degrading performance is affected by the nanocatalyst shape, size, and surface area by providing large active sites, resulting in more redox reactions, ultimately resulting in the breakdown of MB to LMB.

Furthermore, reaction pH influences the reduction process of organic pollutants since reduction is catalyzed well under alkaline conditions compared to acidic ones. In an acidic medium, the electron transfer rate to pollutants is influenced by the secondary reaction of self-hydrolysis of $NaBH_4$ to H_2.[77] Under primary conditions, the surface is negatively charged, so the cationic dye and catalyst exhibit electrostatic attraction, resulting in enhanced dye adsorption.[78] The comparison table of current study with the literature is given in Table 1.

Moreover, the catalytic reduction with $NaBH_4$ is performed because no side reaction starts, which gives convenience in monitoring the absorption spectrum.[82] However, using the $NaBH_4$ reduction process was revealed to be relatively slow during the conversion of MB to harmless, colorless LMB. Even

Table 1. Providing a Comparison of the Current Study with the Literature

materials	synthesis routes	MB degradation	references
CuO NPs	precipitation	74% in 15 min	77
CuO petals/flowers	precipitation	95 and 72% in 24 h	79
CuO nanostructures	hydrothermal	70% after five cycles	80
CS-CuO	precipitation	84% in 30 min	81
CuO:CS-g-PAA	co-precipitation	99.93% in 10 min	present work

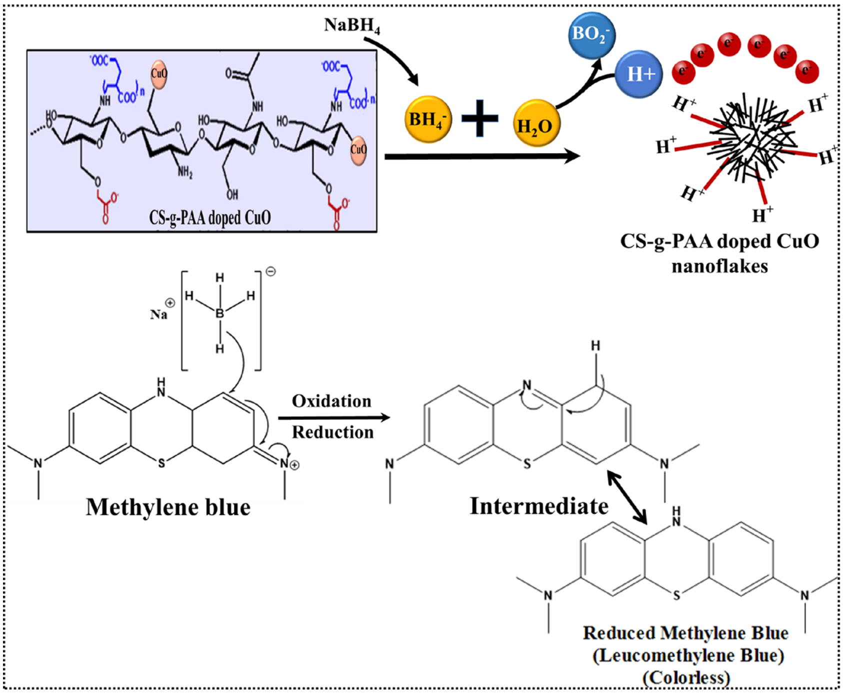

Figure 8. Schematic mechanism for the catalytic activity of MB degradation in the presence of NaBH$_4$ (reducing agent).

though MB reduction using NaBH$_4$ is favorable, it is kinetically limited in the absence of a catalyst, ascribed to a large potential difference between donor and acceptor molecules, as reported earlier.[83] Consequently, potential nanocatalysts improve reaction stability and speed while lowering the activation energy through electron transfer between the donor and acceptor acting as the substrate. This phenomenon is called the "electron relay effect".[84] The reduction of MB follows the typical Langmuir−Hinshelwood model. Adsorption occurred when a catalyst was added to MB along with a reducing agent. Initially, the MB dye and NaBH$_4$ become adsorbed on the catalyst surface while NaBH$_4$ dissociates into BH$_4^-$ and acts as an electron transfer species. The hydrogen gas release from NaBH$_4$ in the reaction mixture leads to the formation of Cu−H on the surface of the catalyst that not only increases the rate of reaction but also decreases the induction time to activate the nanocatalysts by reconstructing its surface. Any impurity on nanocatalysts is removed by this H-flux, and more active sites on the surface are available for the reaction.[85,86] Accordingly, the amount of catalyst utilized in a reaction is critical for providing several active sites. Due to the oxidation−reduction mechanism between the catalyst and the MB, a layer of reductant over catalysts is dispersed, which further accelerates adsorption. As shown in Figure 8, the relay of an electron from donor to acceptor is accelerated by a catalyst that accepts electrons from BH$_4^-$ (donor) and transfers them to MB (acceptor), making the process fast and easy. Afterward, dye molecules are reduced and detached from the catalyst surface. This is a two-electron process since a double bond reduction of the heterocyclic ring reduces the MB electron delocalization length and breaks p-conjugation. Afterward, desorption of the product occurs; this evacuates the active sites, and cycle again continues. As a result, adsorption−desorption equilibrium is quickly restored, and the nanocatalysts get ready for the further reduction run.[86]

A total organic carbon (TOC) assessment of treated water was conducted to estimate the degree of mineralization. The study was performed on CS-g-PAA and (2, 4, and 6%) doped CuO nanomaterials using varying time intervals up to 180 min. This analysis (Figure 9) demonstrated that TOC of synthesized compounds under visible light irradiation reduced continuously with reaction time, and a significant amount of mineralization of the dye was found after 180 min in CS-g-PAA (2%) doped CuO (1:0.02). This reduces CS-g-PAA (4 and 6%) doped CuO owing to different efficiency and degradation rates of CuO.

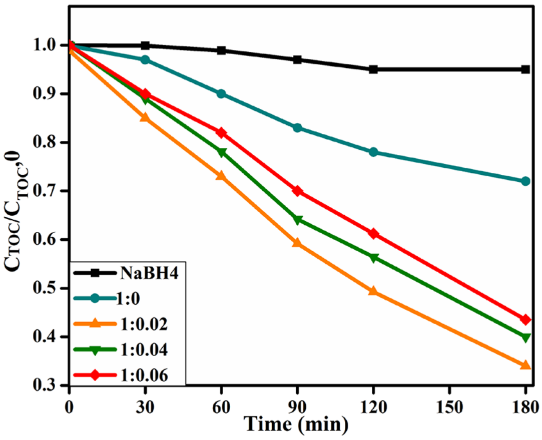

Figure 9. Variation of TOC for synthesized NFs.

In vitro antibacterial activity of pristine CuO, CS-g-PAA, and doped CuO was quantitatively evaluated using inhibition zone measurements against *E. coli* and *S. aureus* by an agar-based diffusion technique (results are displayed in Figure 10a−d and Table 2). At low and high doses, statistically significant ($p < 0.05$) inhibition zones were 4.25−6.15 and 4.40−8.15 mm against *S. aureus* (Figure 11a) and 1.35−4.20 and 2.25−5.25 mm against *E. coli* (Figure 11b). The *S. aureus* efficacy percentages were raised from 46.1 to 66.8 and 47.8 to 88.5%

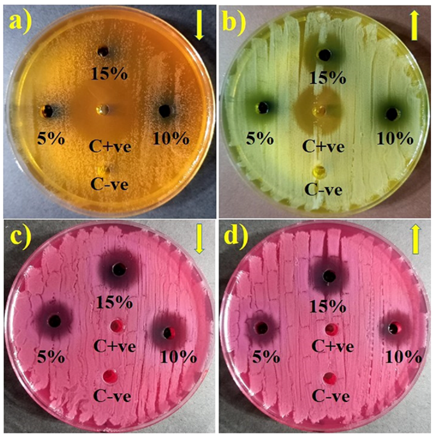

Figure 10. Antibacterial activity with inhibition zones of CuO:CS-g-PAA against (a, b) *S. aureus* and (c, d) *E. coli.*

Table 2. Bactericidal Behavior Results

samples	inhibition zone (mm)[a] 0.5 mg/50 μL	inhibition zone (mm)[a] 1.0 mg/50 μL	inhibition zone (mm)[b] 0.5 mg/50 μL	inhibition zone (mm)[b] 1.0 mg/50 μL
CuO (1:0)	4.25	4.40	1.35	2.25
CS-g-PAA (0:1)	0	1.95	0	0
2% (1:0.02)	0	2.50	2.25	3.25
4% (1:0.04)	3.40	6.20	3.45	4.15
6% (1:0.06)	6.15	8.15	4.20	5.25
ciprofloxacin	9.20	9.20	5.35	5.35
DI water	0	0	0	0

[a]Inhibition zone (mm) for *S. aureus.* [b]Inhibition zone (mm) for *E. coli.*

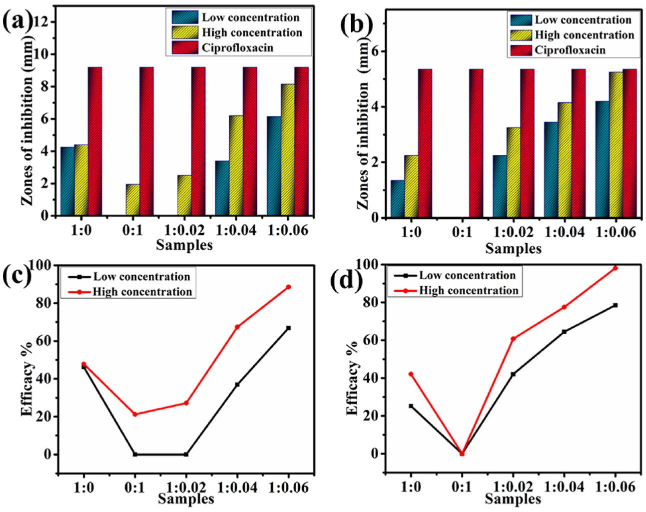

Figure 11. Antibacterial activity with efficacy percentage of CuO:CS-g-PAA against (a, c) *S. aureus* and (b, d) *E. coli.*

(Figure 11c), and *E. coli* percentage efficacies were raised from 25.2 to 78.5 and 42.0 to 98.1% (Figure 11d) for CuO:CS-g-PAA at lowest and highest concentrations, respectively. Ciprofloxacin showed 5.35 and 9.20 mm inhibition areas compared to DI water (0 mm).

The bactericidal action has been linked to free radical formation, cell membrane integrity reduction, and ROS generation ($\cdot O_2^-$, $\cdot HO_2$, $\cdot OH$, and H_2O_2).[87,88] ROS are generated from the electron-donating properties of metal oxides. Furthermore, surface defect sites are thought to generate a considerable amount of ROS (notably superoxide anions) from nanocrystalline CuO.[89] The bacterial cell membrane contains nanometer-sized pores on the surface, so the nanomaterial with an adequate charge and size can penetrate the membrane. These nanomaterials destroy cells by affecting proteins and DNA, ultimately disrupting cell activity.[90] The production of ROS and metal ions released from nanomaterials are meant to generate inhibition zones. In bacteria, CuO has been found to harm the fumarase enzyme.[87] The OH^- (hydroxyl radical) is a high-reactivity oxygen radical that reacts quickly with practically every molecule found in living cells. Those reactions make it easier to combine two OH radicals to generate hydrogen peroxide (H_2O_2). The CuO NFs successfully catalyze intracellular H_2O_2 to hydroxyl ions via a Fenton-like reaction. The breakdown of deoxyribose by hydroxyl ions confirms the NFs' ability to produce hydroxyl ions.[87] Free radicals are produced during the interaction between ROS and outer cell walls that penetrate inner cell membranes and disrupt the cell interior components shown in Figure 12. The cell wall structure affects the bactericidal activity of NFs as multiple layers of peptidoglycan with several pores enable *S. aureus* to be more receptive to intracellular transductions. *E. coli* cell walls are relatively thin, consisting primarily of peptidoglycan and outer layers of phospholipids, lipopolysaccharide, and lipoprotein, which are less responsive to CuO NF attack.[91] Consequently, nanostructured CuO has more potential against *S. aureus* than *E. coli.* Moreover, the bactericidal potential of NFs was influenced by their size, morphological structure, and surface-to-mass ratio.

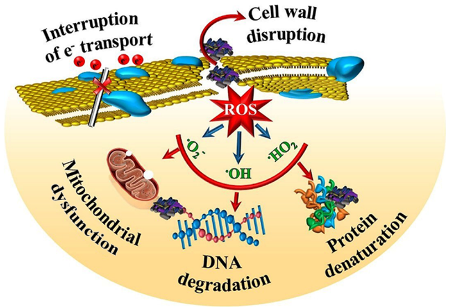

Figure 12. Antibacterial mechanism for as-prepared NFs.

The MIC values for CuO, CS-g-PAA, and doped CuO for *S. aureus* and *E. coli* are listed in Table 3. Even at concentrations as low as 0.056 and 0.012 mg/L, the doped NFs exhibited exceptional antibacterial action against bacterial etiologies, according to the results. As a consequence of solution entrance, full engagement with Cu metal particles, and sluggish ion diffusion, copper ions from Cu cores may be discharged. It

Table 3. CuO, CS-g-PAA, and Doped CuO Nanoflake MIC Values for *S. aureus* and *E. coli*

sample	MIC (mg/L) *S. aureus*	MIC (mg/L) *E. coli*
CuO (1:0)	0.452	0.425
CS-g-PAA (0:1)	0.86	0
2% (1:0.02)	0.648	0.29
4% (1:0.04)	0.26	0.11
6% (1:0.06)	0.056	0.012

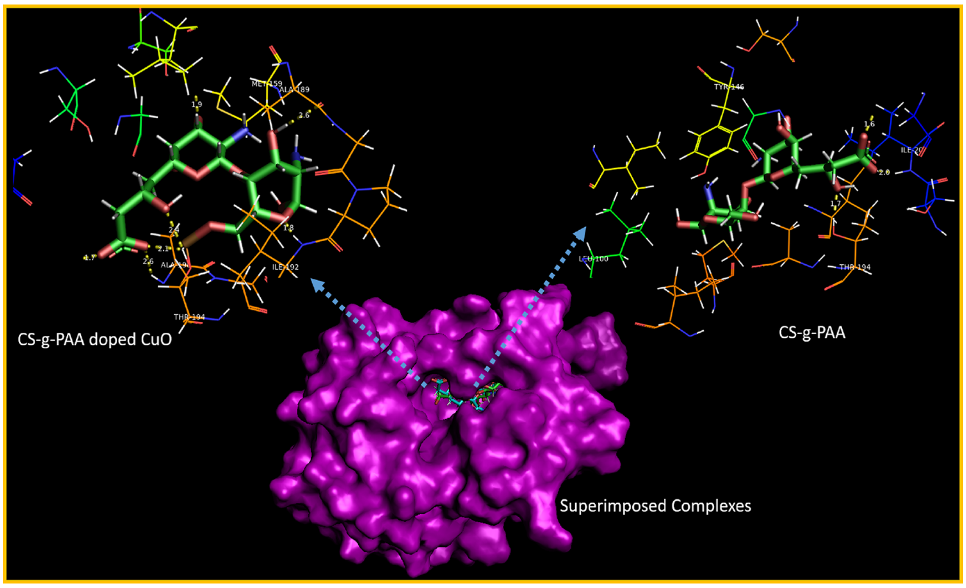

Figure 13. 3D view of the binding interaction pattern of CS-g-PAA and doped CuO NFs inside the active site of $\text{FabI}_{E.\ coli}$.

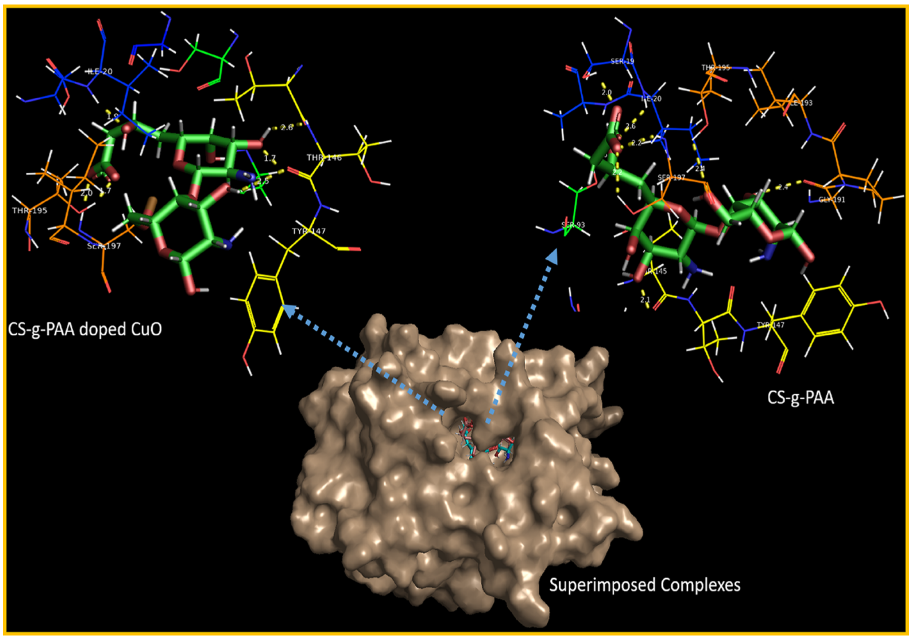

Figure 14. 3D view of the binding interaction pattern of CS-g-PAA and doped CuO NFs inside the active site of $\text{FabI}_{S.\ aureus}$.

is plausible that such doped NFs might assist Cu ions by extending their release time and maintaining antibacterial activity. Compared to *S. aureus*, (1:0.06) doped NFs exhibited a substantial MIC against *E. coli*.

The potential of metal-doped nanoparticles as good bactericidal agents has been studied widely.[92−94] Antibacterial activity of nanoparticles relies on their ability to interact with bacterium either through electrostatic or van der Waals forces or other hydrophobic interactions.[95,96] Enzymes belonging to various biochemical pathways essential for bacterial cells have been reported as key targets for antibiotic discovery. Here, enzymes of the fatty acid biosynthetic pathway have been selected as a possible target to evaluate the inhibition tendency of CS-g-PAA and doped CuO NFs against FabI and FabH from *E. coli* and *S. aureus*.

The best-docked conformation was obtained for CS-g-PAA inside the active pocket of $\text{FabI}_{E.\ coli}$ that revealed a H-bond interaction with Thr194 (1.7 Å) and two H-bonds with Ile20 (1.6 and 2.0 Å) alongside Pi-Pi stacking with Tyr146 with an overall binding score of −7.493 kcal/mol. On the other hand, CS-g-PAA doped CuO nanoflakes (binding score: −9.697 kcal/mol) showed multiple H-bonds with various key amino acids, i.e., Met159 (1.9 Å), Ala189 (2.6 Å), Ile192 (1.8 Å), Thr194 (2.1 and 2.4 Å), and Ala196 (2.6 Å), as depicted in Figure 13.

Both these nanoflakes showed better binding potential against $\text{FabI}_{S.\ aureus}$ as compared to $\text{FabI}_{E.\ coli}$. The CS-g-PAA revealed involvement of Pi-Pi stacking with Tyr147 alongside H-bonded interaction with Ser19 (2.0 Å), Ile20 (2.6 Å), Ser197 (2.2 Å), Gly191 (2.4 Å), and Thr195 (2.4 Å) with a total binding score of −8.937 kcal/mol. A similar trend was

https://doi.org/10.1021/acsomega.2c05625
ACS Omega 2022, 7, 41614−41626

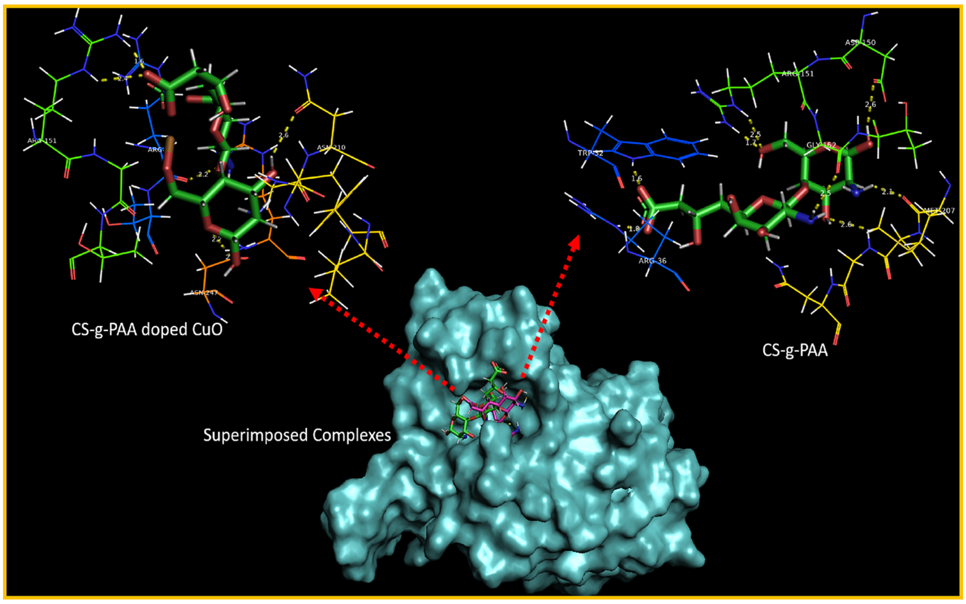

Figure 15. 3D view of the binding interaction pattern of CS-g-PAA and doped CuO NFs inside the active site of FabH$_{E.\ coli}$.

observed in the case of CS-g-PAA doped CuO nanoflake-docked complexes inside the active pocket of FabI$_{S.\ aureus}$, where the best binding score shown was −9.591 kcal/mol. The amino acid residues like Ile20 (2.6 Å), Ser197 (2.2 Å), Thr146 (2.4 Å), Tyr147, and Thr195 (2.4 Å) were involved in H-bond interactions, while the Pi-alkyl interaction was observed with Tyr147, as shown in Figure 14.

In addition, the binding potential of these nanocomposites was also evaluated against another essential enzyme of fatty acid biosynthesis, i.e., FabH$_{E.\ coli}$, where promising binding potential was revealed by CS-g-PAA having a binding score of −10.937 kcal/mol. The main binding interactions involved were H-bonds with Arg36 (1.8 Å), Trp32 (1.6 Å), Asp150 (2.6 Å), Arg151 (1.7 and 2.5 Å), Gly152 (2.5 Å), and Met207 (2.1 Å) alongside the Pi-alkyl interaction with Trp32, as shown in Figure 15. Similarly, CS-g-PAA doped CuO NFs showed H-bonds with Arg36 (2.2 Å), Arg151 (1.6 and 2.4 Å), Asn210 (2.6 Å), and Asn247 (2.2 Å) alongside the metal contact interaction with Gly152 having a total binding score of −7.894 kcal/mol.

4. CONCLUSIONS

CuO, CS-g-PAA, and CS-g-PAA (2, 4, and 6%) doped CuO were prepared by using the co-precipitation method. The doped species in the CuO monoclinic crystal structure was verified by an XRD pattern that also revealed a decrease in crystallite size (28.8, 18.4, 22.1, 19.2, and 19.5 nm) with no change in the crystal system in the synthesized samples. CuO had an interlayer spacing of 0.15 nm, consistent with HR-TEM observation. The FTIR peaks at 1410 and 1640 cm^{-1} confirmed the occurrence of CS-g-PAA in CuO. FE-SEM and TEM revealed NF-like morphology formed by nanorods. The SAED profile of prepared specimens with ring characteristics provided evidence about the polycrystalline nature of nanomaterials. In the presence of NaBH$_4$, CuO and CS-g-PAA doped CuO NFs showed increased catalytic activity against MB. The agar well diffusion method assessed the bactericidal action of samples against pathogenic *S. aureus* and *E. coli*. In silico studies suggested CS-g-PAA and doped CuO nanoflakes as possible inhibitors of FabH and FabI enzymes. Upon doping, improved bactericidal behavior was attributed to enhanced oxygen vacancies that produce hydroxide radicals, singlet oxygen, and ROS in the cell cytoplasm. CuO NFs with natural and synthetic polymers are mostly eco-friendly, cost-beneficial, and effective against bacteria and organic pollutants from polluted water. This study shows that by doping CuO NFs as antimicrobial placebos, potential pathogenic etiologies can be addressed significantly.

AUTHOR INFORMATION

Corresponding Authors

Muhammad Ikram − *Solar Cell Applications Research Lab, Department of Physics, Government College University Lahore, Lahore 54000 Punjab, Pakistan;* orcid.org/0000-0001-7741-789X; Email: dr.muhammadikram@gcu.edu.pk

Walid Nabgan − *Departament d'Enginyeria Química, Universitat Rovira i Virgili, 43007 Tarragona, Spain;* Email: walid.nabgan@urv.cat

Authors

Muhammad Bilal − *Solar Cell Applications Research Lab, Department of Physics, Government College University Lahore, Lahore 54000 Punjab, Pakistan*

Tahira Shujah − *Department of Physics, University of Central Punjab, Lahore 54000 Punjab, Pakistan*

Ali Haider − *Department of Clinical Medicine, Faculty of Veterinary and Animal Sciences, Muhammad Nawaz Shareef, University of Agriculture, 66000 Multan, Punjab, Pakistan*

Sadia Naz − *Tianjin Institute of Industrial Biotechnology, Chinese Academy of Sciences, Tianjin 300308, China*

Anwar Ul-Hamid − *Core Research Facilities, King Fahd University of Petroleum & Minerals, Dhahran 31261, Saudi Arabia;* orcid.org/0000-0002-0259-301X

Misbah Naz − *Department of Chemistry, University of the Education, 54000 Lahore, Pakistan*

Junaid Haider − *Tianjin Institute of Industrial Biotechnology, Chinese Academy of Sciences, Tianjin 300308, China;* orcid.org/0000-0002-2254-1196

https://doi.org/10.1021/acsomega.2c05625
ACS Omega 2022, 7, 41614−41626

Iram Shahzadi − *Punjab University College of Pharmacy, Allama Iqbal Campus, University of the Punjab, Lahore 54000, Pakistan*

Complete contact information is available at: https://pubs.acs.org/10.1021/acsomega.2c05625

Notes

The authors declare no competing financial interest.

■ ACKNOWLEDGMENTS

Authors are grateful to HEC, Pakistan through NRPU-20-17615.

■ REFERENCES

(1) Acisli, O.; Khataee, A.; Karaca, S.; Sheydaei, M. Modification of nanosized natural montmorillonite for ultrasound-enhanced adsorption of Acid Red 17. *Ultrason. Sonochem.* **2016**, *31*, 116−121.

(2) Soltani, R. D. C.; Khataee, A.; Safari, M.; Joo, S. Preparation of bio-silica/chitosan nanocomposite for adsorption of a textile dye in aqueous solutions. *Int. Biodeterior. Biodegrad.* **2013**, *85*, 383−391.

(3) Pandey, S.; Mishra, S. B. Catalytic reduction of p-nitrophenol by using platinum nanoparticles stabilised by guar gum. *Carbohydr. Polym.* **2014**, *113*, 525−531.

(4) Makhado, E.; Motshabi, B. R.; Allouss, D.; Ramohlola, K. E.; Modibane, K. D.; Hato, M. J.; Jugade, R. M.; Shaik, F.; Pandey, S. Development of a ghatti gum/poly (acrylic acid)/TiO2 hydrogel nanocomposite for malachite green adsorption from aqueous media: Statistical optimization using response surface methodology. *Chemosphere* **2022**, *306*, No. 135524.

(5) Sultan, M. Polyurethane for removal of organic dyes from textile wastewater. *Environ. Chem. Lett.* **2017**, *15*, 347−366.

(6) Khataee, A.; Sheydaei, M.; Hassani, A.; Taseidifar, M.; Karaca, S. Sonocatalytic removal of an organic dye using TiO2/Montmorillonite nanocomposite. *Ultrason. Sonochem.* **2015**, *22*, 404−411.

(7) Babaei, A. A.; Khataee, A.; Ahmadpour, E.; Sheydaei, M.; Kakavandi, B.; Alaee, Z. Optimization of cationic dye adsorption on activated spent tea: equilibrium, kinetics, thermodynamic and artificial neural network modeling. *Korean J. Chem. Eng.* **2016**, *33*, 1352−1361.

(8) Pandey, S.; Do, J. Y.; Kim, J.; Kang, M. Fast and highly efficient catalytic degradation of dyes using κ-carrageenan stabilized silver nanoparticles nanocatalyst. *Carbohydr. Polym.* **2020**, *230*, No. 115597.

(9) Sultan, M.; Javeed, A.; Uroos, M.; Imran, M.; Jubeen, F.; Nouren, S.; Saleem, N.; Bibi, I.; Masood, R.; Ahmed, W. Linear and crosslinked Polyurethanes based catalysts for reduction of methylene blue. *J. Hazard. Mater.* **2018**, *344*, 210−219.

(10) Bazrafshan, A. A.; Hajati, S.; Ghaedi, M.; Asfaram, A. Synthesis and characterization of antibacterial chromium iron oxide nanoparticle-loaded activated carbon for ultrasound-assisted wastewater treatment. *Appl. Organomet. Chem.* **2018**, *32*, No. e3981.

(11) Rambabu, K.; Bharath, G.; Banat, F.; Show, P. L. Green synthesis of zinc oxide nanoparticles using Phoenix dactylifera waste as bioreductant for effective dye degradation and antibacterial performance in wastewater treatment. *J. Hazard. Mater.* **2021**, *402*, No. 123560.

(12) Shah, L. A.; Haleem, A.; Sayed, M.; Siddiq, M. Synthesis of sensitive hybrid polymer microgels for catalytic reduction of organic pollutants. *J. Environ. Chem. Eng.* **2016**, *4*, 3492−3497.

(13) Rambabu, K.; Velu, S. Modified polyethersulfone ultrafiltration membrane for the treatment of tannery wastewater. *Int. J. Environ. Stud.* **2016**, *73*, 819−826.

(14) Krishnamoorthy, R.; Sagadevan, V. Polyethylene glycol and iron oxide nanoparticles blended polyethersulfone ultrafiltration membrane for enhanced performance in dye removal studies. *e-Polym.* **2015**, *15*, 151−159.

(15) Pandey, S.; Son, N.; Kang, M. Synergistic sorption performance of karaya gum crosslink poly (acrylamide-co-acrylonitrile)@ metal nanoparticle for organic pollutants. *Int. J. Biol. Macromol.* **2022**, *210*, 300−314.

(16) Pandey, S.; Son, N.; Kim, S.; Balakrishnan, D.; Kang, M. Locust Bean gum-based hydrogels embedded magnetic iron oxide nanoparticles nanocomposite: Advanced materials for environmental and energy applications. *Environ. Res.* **2022**, *214*, No. 114000.

(17) Bhaduri, A.; Kajal. Facile synthesis and characterization of cupric oxide (CuO) nanoparticles: Inexpensive and abundant candidate for light harvesting. *AIP Conf. Proc.* **2019**, *2093*, No. 020047.

(18) Mallakpour, S.; Azadi, E.; Hussain, C. M. Environmentally benign production of cupric oxide nanoparticles and various utilizations of their polymeric hybrids in different technologies. *Coord. Chem. Rev.* **2020**, *419*, No. 213378.

(19) Xu, L.; Srinivasakannan, C.; Peng, J.; Zhang, L.; Zhang, D. Synthesis of Cu-CuO nanocomposite in microreactor and its application to photocatalytic degradation. *J. Alloys Compd.* **2017**, *695*, 263−269.

(20) Babu, A. T.; Antony, R. Green synthesis of silver doped nano metal oxides of zinc & copper for antibacterial properties, adsorption, catalytic hydrogenation & photodegradation of aromatics. *J. Environ. Chem. Eng.* **2019**, *7*, No. 102840.

(21) Junior, O. S.; Monteiro, A.; Oliveira, J.; Araújo, A.; Silva, D.; Kulesza, J.; Barros, B. Coordination polymer-derived CuO catalysts for oxidative degradation of methylene blue. *Mater. Chem. Phys.* **2019**, *235*, No. 121737.

(22) He, X.; Yang, D.-P.; Zhang, X.; Liu, M.; Kang, Z.; Lin, C.; Jia, N.; Luque, R. Waste eggshell membrane-templated CuO-ZnO nanocomposites with enhanced adsorption, catalysis and antibacterial properties for water purification. *Chem. Eng. J.* **2019**, *369*, 621−633.

(23) Cai, Y.; Yang, F.; Wu, L.; Shu, Y.; Qu, G.; Fakhri, A.; Gupta, V. K. Hydrothermal-ultrasonic synthesis of CuO nanorods and CuWO4 nanoparticles for catalytic reduction, photocatalysis activity, and antibacterial properties. *Mater. Chem. Phys.* **2021**, *258*, No. 123919.

(24) Bhavyasree, P.; Xavier, T. Adsorption studies of Methylene Blue, Coomassie Brilliant Blue, and Congo Red dyes onto CuO/C nanocomposites synthesized via Vitex negundo Linn leaf extract. *Curr. Res. Green Sustainable Chem.* **2021**, *4*, No. 100161.

(25) Zhang, T.; Li, W.; Guo, Q.; Wang, Y.; Li, C. Preparation of a Heterogeneous Catalyst CuO-Fe2O3/CTS-ATP and Degradation of Methylene Blue and Ciprofloxacin. *Coatings* **2022**, *12*, 559.

(26) Dasauni, K.; Nailwal, T.; Nenavathu, B. P.Facile synthesis and characterization of Te-doped CuO nanoparticles for increased antibacterial and photocatalytic activity. *Mater. Today: Proc.***2022**.

(27) Khan, J.; Siddiq, M.; Akram, B.; Ashraf, M. A. In-situ synthesis of CuO nanoparticles in P (NIPAM-co-AAA) microgel, structural characterization, catalytic and biological applications. *Arabian J. Chem.* **2018**, *11*, 897−909.

(28) Khapre, M.; Shekhawat, A.; Saravanan, D.; Pandey, S.; Jugade, R. Mesoporous Fe−Al-doped cellulose for the efficient removal of reactive dyes. *Mater. Adv.* **2022**, *3*, 3278−3285.

(29) Zayed, M. F.; Eisa, W. H.; Hosam, A. E. M.; Abou Zeid, A. M. Spectroscopic investigation of chitosan-supported Cu2O/CuO nanocomposite; a separable catalyst for water-pollutants degradation. *J. Alloys Compd.* **2020**, *835*, No. 155306.

(30) Iqbal, S.; Javed, M.; Bahadur, A.; Qamar, M. A.; Ahmad, M.; Shoaib, M.; Raheel, M.; Ahmad, N.; Akbar, M. B.; Li, H. Controlled synthesis of Ag-doped CuO nanoparticles as a core with poly(acrylic acid) microgel shell for efficient removal of methylene blue under visible light. *J. Mater. Sci.: Mater. Electron.* **2020**, *31*, 8423−8435.

(31) Sarkar, S.; Guibal, E.; Quignard, F.; SenGupta, A. K. Polymer-supported metals and metal oxide nanoparticles: synthesis, characterization, and applications. *J. Nanopart. Res.* **2012**, *14*, 715.

(32) Nechita, P. Applications of chitosan in wastewater treatment. *Biol. Act. Appl. Mar. Polysaccharides* **2017**, *1*, 209−228.

(33) Liu, Z.; Bai, H.; Sun, D. D. Facile fabrication of porous chitosan/TiO 2/Fe 3 O 4 microspheres with multifunction for water purifications. *New J. Chem.* **2011**, *35*, 137−140.

(34) Kausar, A. Poly(acrylic acid) nanocomposites: Design of advanced materials. *J. Plast. Film Sheeting* **2021**, *37*, 409−428.

(35) Ma, Y.; Dong, J.; Bhattacharjee, S.; Wijeratne, S.; Bruening, M. L.; Baker, G. L. Increased Protein Sorption in Poly(acrylic acid)-Containing Films through Incorporation of Comb-Like Polymers and Film Adsorption at Low pH and High Ionic Strength. *Langmuir* **2013**, *29*, 2946−2954.

(36) Zhang, J.; Wang, Q.; Wang, A. Synthesis and characterization of chitosan-g-poly(acrylic acid)/attapulgite superabsorbent composites. *Carbohydr. Polym.* **2007**, *68*, 367−374.

(37) Yu, Z.; Dang, Q.; Liu, C.; Cha, D.; Zhang, H.; Zhu, W.; Zhang, Q.; Fan, B. Preparation and characterization of poly(maleic acid)-grafted cross-linked chitosan microspheres for Cd(II) adsorption. *Carbohydr. Polym.* **2017**, *172*, 28−39.

(38) Zhang, L.; Tang, S.; He, F.; Liu, Y.; Mao, W.; Guan, Y. Highly efficient and selective capture of heavy metals by poly(acrylic acid) grafted chitosan and biochar composite for wastewater treatment. *Chem. Eng. J.* **2019**, *378*, No. 122215.

(39) Bazzazzadeh, A.; Dizaji, B. F.; Kianinejad, N.; Nouri, A.; Irani, M. Fabrication of poly(acrylic acid) grafted-chitosan/polyurethane/magnetic MIL-53 metal organic framework composite core-shell nanofibers for co-delivery of temozolomide and paclitaxel against glioblastoma cancer cells. *Int. J. Pharm.* **2020**, *587*, No. 119674.

(40) Zhao, Y.; Zhu, J.-J.; Hong, J.-M.; Bian, N.; Chen, H.-Y. Microwave-Induced Polyol-Process Synthesis of Copper and Copper Oxide Nanocrystals with Controllable Morphology. *Eur. J. Inorg. Chem.* **2004**, *2004*, 4072−4080.

(41) Wang, S.; Huang, X.; He, Y.; Huang, H.; Wu, Y.; Hou, L.; Liu, X.; Yang, T.; Zou, J.; Huang, B. Synthesis, growth mechanism and thermal stability of copper nanoparticles encapsulated by multi-layer graphene. *Carbon* **2012**, *50*, 2119−2125.

(42) Lin, S. K.; Cheng, W. T. Fabrication and characterization of colloidal silver nanoparticle via photochemical synthesis. *Mater. Lett.* **2020**, *261*, No. 127077.

(43) Xiao, X.; Zhu, Y.; Liao, J.; Wang, T.; Sun, W.; Tong, Z. High-efficient and synergetic antibacterial nanocomposite hydrogel with quaternized chitosan/Ag nanoparticles prepared by one-pot UV photochemical synthesis. *Biopolymers* **2020**, *111*, No. e23354.

(44) Wu, W.; Jiang, C. Z.; Roy, V. A. L. Designed synthesis and surface engineering strategies of magnetic iron oxide nanoparticles for biomedical applications. *Nanoscale* **2016**, *8*, 19421−19474.

(45) Hu, Y.; Jiang, X.; Ding, Y.; Ge, H.; Yuan, Y.; Yang, C. Synthesis and characterization of chitosan−poly(acrylic acid) nanoparticles. *Biomaterials* **2002**, *23*, 3193−3201.

(46) McKinney, D. C.; Eyermann, C. J.; Gu, R.-F.; Hu, J.; Kazmirski, S. L.; Lahiri, S. D.; McKenzie, A. R.; Shapiro, A. B.; Breault, G. Antibacterial FabH Inhibitors with Mode of Action Validated in Haemophilus influenzae by in Vitro Resistance Mutation Mapping. *ACS Infect. Dis.* **2016**, *2*, 456−464.

(47) Seefeld, M. A.; Miller, W. H.; Newlander, K. A.; Burgess, W. J.; DeWolf, W. E.; Elkins, P. A.; Head, M. S.; Jakas, D. R.; Janson, C. A.; Keller, P. M.; Manley, P. J.; Moore, T. D.; Payne, D. J.; Pearson, S.; Polizzi, B. J.; Qiu, X.; Rittenhouse, S. F.; Uzinskas, I. N.; Wallis, N. G.; Huffman, W. F. Indole Naphthyridinones as Inhibitors of Bacterial Enoyl-ACP Reductases FabI and FabK. *J. Med. Chem.* **2003**, *46*, 1627−1635.

(48) Fage, C. D.; Lathouwers, T.; Vanmeert, M.; Gao, L.-J.; Vrancken, K.; Lammens, E.-M.; Weir, A. N. M.; Degroote, R.; Cuppens, H.; Kosol, S.; Simpson, T. J.; Crump, M. P.; Willis, C. L.; Herdewijn, P.; Lescrinier, E.; Lavigne, R.; Anné, J.; Masschelein, J. The Kalimantacin Polyketide Antibiotics Inhibit Fatty Acid Biosynthesis in Staphylococcus aureus by Targeting the Enoyl-Acyl Carrier Protein Binding Site of FabI. *Angew. Chem., Int. Ed.* **2020**, *59*, 10549−10556.

(49) Abagyan, R.; Totrov, M. Biased Probability Monte Carlo Conformational Searches and Electrostatic Calculations for Peptides and Proteins. *J. Mol. Biol.* **1994**, *235*, 983−1002.

(50) Domingues, R. P.; Rodrigues, M. S.; Lopes, C.; Pedrosa, P.; Alves, E.; Barradas, N. P.; Borges, J.; Vaz, F. Thin films composed of metal nanoparticles (Au, Ag, Cu) dispersed in AlN: The influence of composition and thermal annealing on the structure and plasmonic response. *Thin Solid Films* **2019**, *676*, 12−25.

(51) Qi, J. Q.; Tian, H. Y.; Li, L. T.; Chan, H. L. W. Fabrication of CuO nanoparticle interlinked microsphere cages by solution method. *Nanoscale Res. Lett.* **2007**, *2*, 107.

(52) Ghosh, S.; Avasthi, D. K.; Shah, P.; Ganesan, V.; Gupta, A.; Sarangi, D.; Bhattacharya, R.; Assmann, W. Deposition of thin films of different oxides of copper by RF reactive sputtering and their characterization. *Vacuum* **2000**, *57*, 377−385.

(53) Kyzas, G. Z.; Bikiaris, D. N.; Seredych, M.; Bandosz, T. J.; Deliyanni, E. A. Removal of dorzolamide from biomedical waste-waters with adsorption onto graphite oxide/poly(acrylic acid) grafted chitosan nanocomposite. *Bioresour. Technol.* **2014**, *152*, 399−406.

(54) Govindan, S.; Nivethaa, E. A. K.; Saravanan, R.; Narayanan, V.; Stephen, A. Synthesis and characterization of chitosan−silver nanocomposite. *Appl. Nanosci.* **2012**, *2*, 299−303.

(55) Liu, A.; Luong, H. B.; Kim, J. C.; Lizhu, L.Preparation and characterization of polymer -copper composites by electrical explosion of wire. *In Proceedings of 2011 6th International Forum on Strategic Technology*, 22−24 Aug. 2011; 2011; pp. 29−32.

(56) TODICA, M.; Stefan, T.; SIMON, S.; BALASZ, I.; DARABAN, L. UV-vis and XRD investigation of graphite-doped poly (acrylic) acid membranes. *Turk. J. Phys.* **2014**, *38*, 261−267.

(57) Sathiyavimal, S.; Vasantharaj, S.; Kaliannan, T.; Pugazhendhi, A. Eco-biocompatibility of chitosan coated biosynthesized copper oxide nanocomposite for enhanced industrial (Azo) dye removal from aqueous solution and antibacterial properties. *Carbohydr. Polym.* **2020**, *241*, No. 116243.

(58) Theivasanthi, T.; Alagar, M., Konjac bio-molecules assisted, rod-spherical shaped lead nano powder synthesized by electrolytic process and its characterization studies. *arXiv preprint arXiv:1212.5795*2012.

(59) Halder, M.; Islam, M. M.; Ansari, Z.; Ahammed, S.; Sen, K.; Islam, S. M. Biogenic Nano-CuO-Catalyzed Facile C−N Cross-Coupling Reactions: Scope and Mechanism. *ACS Sustainable Chem. Eng.* **2017**, *5*, 648−657.

(60) Sundar, S.; Venkatachalam, G.; Kwon, S. J. Biosynthesis of Copper Oxide (CuO) Nanowires and Their Use for the Electrochemical Sensing of Dopamine. *Nanomaterials* **2018**, *8*, 823.

(61) Dubal, D. P.; Gund, G. S.; Lokhande, C. D.; Holze, R. CuO cauliflowers for supercapacitor application: Novel potentiodynamic deposition. *Mater. Res. Bull.* **2013**, *48*, 923−928.

(62) Ethiraj, A. S.; Kang, D. J. Synthesis and characterization of CuO nanowires by a simple wet chemical method. *Nanoscale Res. Lett.* **2012**, *7*, 70.

(63) Debbichi, L.; Marco de Lucas, M. C.; Pierson, J. F.; Krüger, P. Vibrational Properties of CuO and Cu4O3 from First-Principles Calculations, and Raman and Infrared Spectroscopy. *J. Phys. Chem. C* **2012**, *116*, 10232−10237.

(64) Ortega-Ortiz, H.; Gutiérrez-Rodríguez, B.; Cadenas-Pliego, G.; Jimenez, L. I. Antibacterial activity of chitosan and the interpolyelectrolyte complexes of poly (acrylic acid)-chitosan. *Braz. Arch. Biol. Technol.* **2010**, *53*, 623−628.

(65) Mahmoud, A. E. D.; Al-Qahtani, K. M.; Alflaij, S. O.; Al-Qahtani, S. F.; Alsamhan, F. A. Green copper oxide nanoparticles for lead, nickel, and cadmium removal from contaminated water. *Sci. Rep.* **2021**, *11*, 12547.

(66) Bibi, H.; Iqbal, M.; Wahab, H.; Öztürk, M.; Ke, F.; Iqbal, Z.; Khan, M. I.; Alghanem, S. M. Green synthesis of multifunctional carbon coated copper oxide nanosheets and their photocatalytic and antibacterial activities. *Sci. Rep.* **2021**, *11*, 10781.

(67) Epping, R.; Panne, U.; Hiller, W.; Gruendling, T.; Staal, B.; Lang, C.; Lamprou, A.; Falkenhagen, J. Simultaneous characterization of poly(acrylic acid) and polysaccharide polymers and copolymers. *Anal. Sci. Adv.* **2020**, *1*, 34−45.

(68) Bandara, S.; Carnegie, C.-A.; Johnson, C.; Akindoju, F.; Williams, E.; Swaby, J. M.; Oki, A.; Carson, L. E. Synthesis and

characterization of Zinc/Chitosan-Folic acid complex. *Heliyon* **2018**, *4*, No. e00737.

(69) Gondal, M. A.; Qahtan, T. F.; Dastageer, M. A.; Saleh, T. A.; Maganda, Y. W.; Anjum, D. H. Effects of oxidizing medium on the composition, morphology and optical properties of copper oxide nanoparticles produced by pulsed laser ablation. *Appl. Surf. Sci.* **2013**, *286*, 149−155.

(70) Chand, P.; Gaur, A.; Kumar, A.; Gaur, U. K. Effect of NaOH molar concentration on morphology, optical and ferroelectric properties of hydrothermally grown CuO nanoplates. *Mater. Sci. Semicond. Process.* **2015**, *38*, 72−80.

(71) Siddiqui, H.; Qureshi, M. S.; Haque, F. Z. Surfactant assisted wet chemical synthesis of copper oxide (CuO) nanostructures and their spectroscopic analysis. *Optik* **2016**, *127*, 2740−2747.

(72) Karthikeyan, C.; Varaprasad, K.; Venugopal, S. K.; Shakila, S.; Venkatraman, B. R.; Sadiku, R. Biocidal (bacterial and cancer cells) activities of chitosan/CuO nanomaterial, synthesized via a green process. *Carbohydr. Polym.* **2021**, *259*, No. 117762.

(73) Tichapondwa, S. M.; Newman, J.; Kubheka, O. Effect of TiO2 phase on the photocatalytic degradation of methylene blue dye. *Phys. Chem. Earth, Parts A/B/C* **2020**, *118*, No. 102900.

(74) Deka, P.; Hazarika, A.; Deka, R. C.; Bharali, P. Influence of CuO morphology on the enhanced catalytic degradation of methylene blue and methyl orange. *RSC Adv.* **2016**, *6*, 95292−95305.

(75) Shrestha, K. M.; Sorensen, C. M.; Klabunde, K. J. Synthesis of CuO nanorods, reduction of CuO into Cu nanorods, and diffuse reflectance measurements of CuO and Cu nanomaterials in the near infrared region. *J. Phys. Chem. C* **2010**, *114*, 14368−14376.

(76) Srivastava, V.; Choubey, A. K. Investigation of adsorption of organic dyes present in wastewater using chitosan beads immobilized with biofabricated CuO nanoparticles. *J. Mol. Struct.* **2021**, *1242*, No. 130749.

(77) Benhadria, N.; Hachemaoui, M.; Zaoui, F.; Mokhtar, A.; Boukreris, S.; Attar, T.; Belarbi, L.; Boukoussa, B. Catalytic reduction of methylene blue dye by copper oxide nanoparticles. *J. Cluster Sci.* **2022**, *33*, 249−260.

(78) Nguyen Thi Thu, T.; Nguyen Thi, N.; Tran Quang, V.; Nguyen Hong, K.; Nguyen Minh, T.; Le Thi Hoai, N. Synthesis, characterisation, and effect of pH on degradation of dyes of copper-doped TiO2. *J. Exp. Nanosci.* **2016**, *11*, 226−238.

(79) Zaman, S.; Zainelabdin, A.; Amin, G.; Nur, O.; Willander, M. Efficient catalytic effect of CuO nanostructures on the degradation of organic dyes. *J. Phys. Chem. Solids* **2012**, *73*, 1320−1325.

(80) Ye, Y.; Wan, J.; Li, Q.; Huang, Y.; Pan, F.; Xia, D. Catalytic oxidation of dyeing wastewater by copper oxide activating persulfate: performance, mechanism and application. *Int. J. Environ. Res.* **2021**, *15*, 1−10.

(81) Haldorai, Y.; Shim, J.-J. Multifunctional chitosan-copper oxide hybrid material: photocatalytic and antibacterial activities. *Int. J. Photoenergy* **2013**, *2013*, 1.

(82) Rajamanikandan, R.; Shanmugaraj, K.; Ilanchelian, M. Concentration Dependent Catalytic Activity of Glutathione Coated Silver Nanoparticles for the Reduction of 4-Nitrophenol and Organic Dyes. *J. Cluster Sci.* **2017**, *28*, 1009−1023.

(83) Hashimi, A. S.; Nohan, M. A. N. M.; Chin, S. X.; Zakaria, S.; Chia, C. H. Rapid Catalytic Reduction of 4-Nitrophenol and Clock Reaction of Methylene Blue using Copper Nanowires. *Nanomaterials* **2019**, *9*, 936.

(84) Saad, A.; Snoussi, Y.; Abderrabba, M.; Chehimi, M. M. Ligand-modified mesoporous silica SBA-15/silver hybrids for the catalyzed reduction of methylene blue. *RSC Adv.* **2016**, *6*, 57672−57682.

(85) Naz, M.; Rafiq, A.; Ikram, M.; Haider, A.; Ahmad, S. O. A.; Haider, J.; Naz, S. Elimination of dyes by catalytic reduction in the absence of light: A review. *J. Mater. Sci.* **2021**, *56*, 15572−15608.

(86) Begum, R.; Najeeb, J.; Sattar, A.; Naseem, K.; Irfan, A.; Al-Sehemi, A. G.; Farooqi, Z. H. Chemical reduction of methylene blue in the presence of nanocatalysts: a critical review. *Rev. Chem. Eng.* **2020**, *36*, 749−770.

(87) Meghana, S.; Kabra, P.; Chakraborty, S.; Padmavathy, N. Understanding the pathway of antibacterial activity of copper oxide nanoparticles. *RSC Adv.* **2015**, *5*, 12293−12299.

(88) Jadhav, S.; Gaikwad, S.; Nimse, M.; Rajbhoj, A. Copper Oxide Nanoparticles: Synthesis, Characterization and Their Antibacterial Activity. *J. Cluster Sci.* **2011**, *22*, 121−129.

(89) Rensing, C.; Grass, G. Escherichia coli mechanisms of copper homeostasis in a changing environment. *FEMS Microbiol. Rev.* **2003**, *27*, 197−213.

(90) Chen, C. Z.; Cooper, S. L. Interactions between dendrimer biocides and bacterial membranes. *Biomaterials* **2002**, *23*, 3359−3368.

(91) Zoolfakar, A. S.; Rani, R. A.; Morfa, A. J.; O'Mullane, A. P.; Kalantar-zadeh, K. Nanostructured copper oxide semiconductors: a perspective on materials, synthesis methods and applications. *J. Mater. Chem. C* **2014**, *2*, 5247−5270.

(92) Altaf, S.; Haider, A.; Naz, S.; Ul-Hamid, A.; Haider, J.; Imran, M.; Shahzadi, A.; Naz, M.; Ajaz, H.; Ikram, M. Comparative Study of Selenides and Tellurides of Transition Metals (Nb and Ta) with Respect to its Catalytic, Antimicrobial, and Molecular Docking Performance. *Nanoscale Res. Lett.* **2020**, *15*, 144.

(93) Arularasu, M. V.; Harb, M.; Sundaram, R. Synthesis and characterization of cellulose/TiO2 nanocomposite: Evaluation of in vitro antibacterial and in silico molecular docking studies. *Carbohydr. Polym.* **2020**, *249*, No. 116868.

(94) Ikram, M.; Hassan, J.; Raza, A.; Haider, A.; Naz, S.; Ul-Hamid, A.; Haider, J.; Shahzadi, I.; Qamar, U.; Ali, S. Photocatalytic and bactericidal properties and molecular docking analysis of TiO 2 nanoparticles conjugated with Zr for environmental remediation. *RSC Adv.* **2020**, *10*, 30007−30024.

(95) Dakal, T. C.; Kumar, A.; Majumdar, R. S.; Yadav, V. Mechanistic basis of antimicrobial actions of silver nanoparticles. *Front. Microbiol.* **2016**, *7*, 1831.

(96) Shahzadi, I.; Islam, M.; Saeed, H.; Haider, A.; Shahzadi, A.; Haider, J.; Ahmed, N.; Ul-Hamid, A.; Nabgan, W.; Ikram, M.; Rathore, H. A. Formation of biocompatible MgO/cellulose grafted hydrogel for efficient bactericidal and controlled release of doxorubicin. *Int. J. Biol. Macromol.* **2022**, 1277.